ACS Energy LETTERS

http://pubs.acs.org/journal/aelccp

LETTER

Sulfur-Infused Hole Transport Materials to Overcome Performance-Limiting Transport in Colloidal Quantum Dot Solar Cells

Arlene Chiu, Eric Rong, Christianna Bambini, Yida Lin, Chengchangfeng Lu, and Susanna M. Thon*

Cite This: *ACS Energy Lett.* 2020, 5, 2897–2904

Read Online

ACCESS | Metrics & More | Article Recommendations | Supporting Information

ABSTRACT: Colloidal quantum dot (CQD) solar cells have benefited from rapidly rising single-junction efficiencies in recent years and have shown promise in multijunction and color-tuned applications. However, within the context of next-generation solar cells, CQD photovoltaics still have an efficiency deficit compared to mature technologies. Here, we use one-dimensional optoelectronic solar cell simulations to show that much of this efficiency deficit in the highest-performing PbS CQD solar cells can be attributed to the hole transport layer (HTL). We find that increasing both the doping density and, counterintuitively, the electron mobility in this layer should have the largest impact on performance, attributed to the nontrivial role that the HTL plays in photon absorption. We use stoichiometry control through sulfur infusion of the standard CQD HTL materials to improve the carrier mobilities and doping density. This work resulted in a clear performance improvement, to 10.4% power conversion efficiency in the best device.

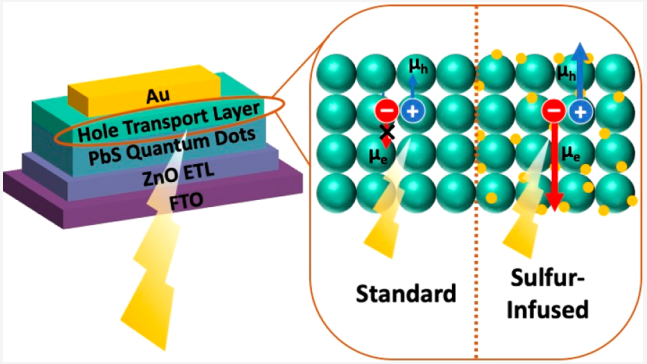

Semiconductor colloidal quantum dots (CQDs) are nanomaterials of interest for optoelectronic applications because they exhibit size-dependent optical and electronic properties due to quantum confinement effects.[1−4] PbS CQDs are of particular interest for photovoltaics because of their tunable absorption throughout the near-infrared;[5] their earth-abundant materials basis; and their amenability to a variety of solution-processed, scalable fabrication methods,[6,7] all of which enable their promising applications in multi-junction solar cells,[8,9] color-tuned devices for building-integrated photovoltaics,[10,11] and flexible electronics.[12,13] The field of PbS CQD photovoltaics has achieved power conversion efficiencies (PCEs) of over 13%[14] attributed to improvements in materials,[15,16] device architectures,[17,18] and surface ligand engineering.[19,20] Although advances in efficiency continue apace, the best-performing silicon, thin-film chalcogenide (CdTe and Cu(In,Ga)Se_2 (CIGS)), and perovskite solar cells have surpassed 20% PCE.[21] Therefore, higher efficiencies are needed in CQD solar cells in order for them to be competitive with other technologies.

The solar cell layer structure used in the highest-efficiency PbS CQD solar cells[22] is shown in Figure 1c. The absorbing layer consists of oleic acid-capped CQDs that have undergone a solution-phase ligand exchange with PbX_2 (X = Br, I) and ammonium acetate ("PbS-PbX_2" in the diagram). ZnO serves as the n-type electron transport layer (ETL) in CQD solar cells, which effectively blocks hole transport while efficiently transporting electrons through. This material has been studied in depth[23,24] and is generally considered to have a high doping density up to 10^{18} cm^{-3} as well as ideal band alignment with the PbS CQD absorbing materials.[25] The hole transport layer (HTL) is meant to minimize leakage and recombination by facilitating hole transport to, and band alignment with, the deep work function metal top contact, while also blocking electron transport.[26] Current high-performing CQD solar cells use a thin (<100 nm) layer of PbS CQDs with solid-state-exchanged ethanedithiol (EDT) ligands as the p-type HTL.[14] This material exhibits low carrier mobilities and relatively low doping densities, making it presumably a critical barrier in the highest-performing CQD solar cell devices.[27] Development of

Received: July 23, 2020
Accepted: August 18, 2020
Published: August 18, 2020

https://dx.doi.org/10.1021/acsenergylett.0c01586
ACS Energy Lett. 2020, 5, 2897–2904

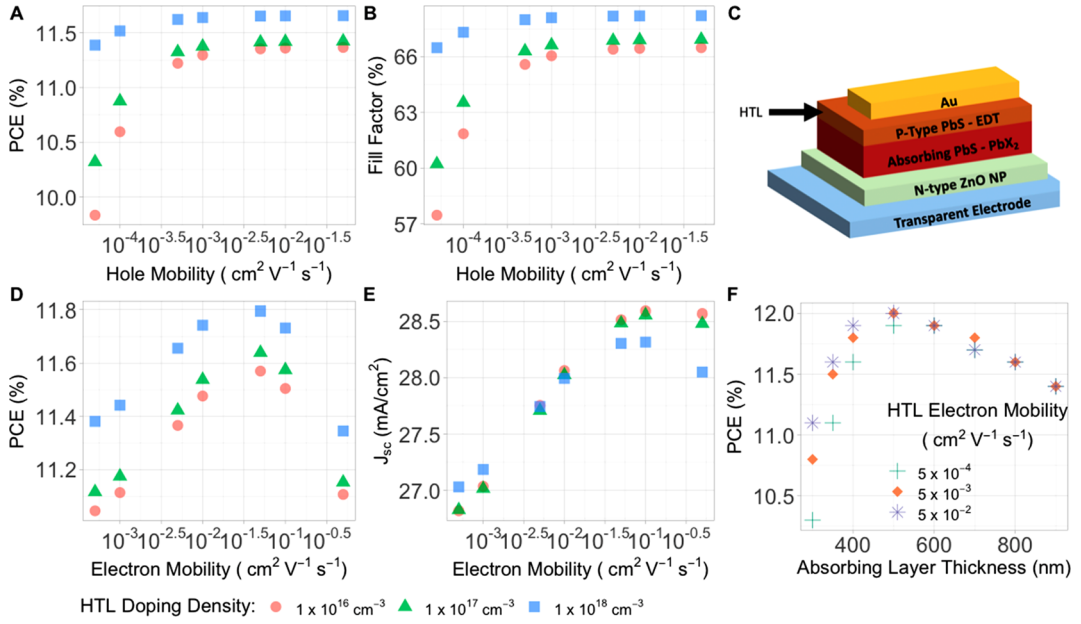

Figure 1. SCAPS simulations results: (a and b) PCE and fill factor, respectively, as a function of HTL hole mobility with a constant HTL electron mobility of 5×10^{-3} cm^2 V^{-1} s^{-1} and HTL doping densities of 1×10^{16} (red circles), 1×10^{17} (green triangles), and 1×10^{18} (blue squares). (c) Diagram of the CQD solar cell layer structure consisting of a bottom transparent substrate (not shown), a transparent electrode (fluorine-doped tin oxide in this work), a wide bandgap electron-extracting n-type semiconductor (ZnO), an intrinsic bulk absorbing PbS-PbX$_2$ (X = Br, I) CQD thin film, a thin hole-extracting p-type PbS CQD film treated with ethanedithiol (EDT) ligands, and a top evaporated Au contact. The hole-transporting layer (HTL) is indicated by a black arrow. (d and e) PCE and J_{sc}, respectively, as a function of HTL electron mobility with a constant hole mobility of 5×10^{-2} cm^2 V^{-1} s^{-1}. (f) PCE as a function of absorbing layer thickness for HTL electron mobilities of 5×10^{-4} cm^2 V^{-1} s^{-1} (green crosses), 5×10^{-3} cm^2 V^{-1} s^{-1} (orange diamonds), and 5×10^{-2} cm^2 V^{-1} s^{-1} (purple stars).

the HTL has been more recent and focused on new ligand strategies, which have achieved promising results.[28,29]

In this work, we elucidate the impact of the HTL electronic properties, including carrier mobilities, doping density, and energy band levels, on device efficiency using one-dimensional Solar Cell Capacitance Simulator (SCAPS) calculations.[30] Using the insights gained from this study, we introduce elemental sulfur as a means of performing stoichiometric control of the HTL. Our new HTL material shows increased p-type character[31] and improved CQD photovoltaic efficiencies via sulfur surface passivation, which facilitates higher electron mobilities for photogenerated electrons within the HTL. We use capacitance−voltage (Cap−V) measurements to obtain doping densities, space-charge-limited current (SCLC) measurements to acquire carrier mobilities, and current density−voltage (J−V) measurements under simulated solar illumination to measure solar cell device performance parameters. By increasing the doping density and electron mobility of our HTLs through stoichiometry tuning, we achieved a clear improvement in device performance, from a maximum of 9.3% to 10.4% power conversion efficiency. The improvement of the HTL that we demonstrate could have immediate applications in flexible, wearable, building-integrated, and multijunction photovoltaics. Our study also provides insights that can be used to further improve the performance of CQD solar cells, including the necessity of improving transport in the absorbing layer so that it can be made thick enough to prevent photogeneration in the HTL.

In order to determine the limiting factors in the performance of CQD solar cells, we undertook a variational computational study of critical parameters associated with the HTL. Specifically, we used SCAPS to study the effects of the HTL doping density and both electron and hole mobility, as well as the band alignment between the absorbing layer and the HTL, on the performance of the CQD solar cell. SCAPS is a one-dimensional solar cell simulator that takes parameters such as carrier mobilities, doping densities, and recombination center densities as inputs and uses the drift−diffusion and Poisson's equations to calculate J−V characteristics and energy band diagrams.[30] We used materials parameters based on literature values for CQD solar cells detailed in the Supporting Information (Table S1)[32−34] and layer thicknesses of 350 nm for the PbS-PbX$_2$ absorbing layer and 60 nm for the PbS-EDT HTL layer, based on our own thickness optimization studies. We varied the doping density in the HTL from 10^{16} to 10^{18} cm^{-3}, the electron mobility from 5×10^{-4} to 5×10^{-1} cm^2 V^{-1} s^{-1}, and the hole mobility from 5×10^{-5} to 5×10^{-2} cm^2 V^{-1} s^{-1}. These parameter ranges represented reasonable values based on our own results and results from the literature[35−38] for the HTL. The full results for all parameter combinations are detailed in the Supporting Information (Figure S1).

Figure 1 shows the simulation results for the doping density, hole mobility, and electron mobility of the HTL. We note that, in general, the device PCE increases with an increase in doping density, electron mobility, and hole mobility of the HTL. In Figure 1a,b, the PCE and fill factor (FF) are plotted as a function of HTL hole mobility for different values of the HTL doping density, with the electron mobility set to our experimental value of 5×10^{-3} cm^2 V^{-1} s^{-1}. The observed increases in PCE with both increasing hole mobility and doping density can largely be attributed to increases in device FF, which generally tracks with the expected decrease in resistivity associated with higher doping densities. This effect

https://dx.doi.org/10.1021/acsenergylett.0c01586
ACS Energy Lett. 2020, 5, 2897−2904

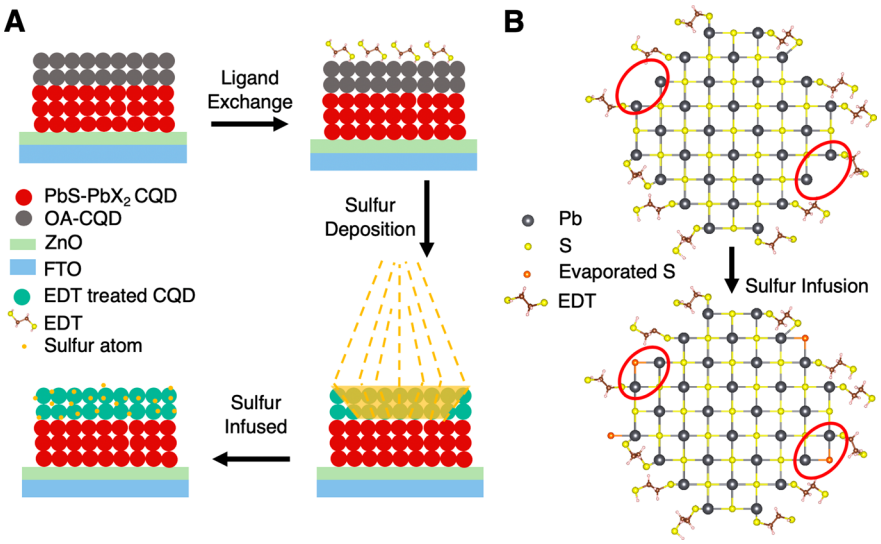

Figure 2. (a) Schematic of the sulfur-infused hole transport layer fabrication process. A PbS CQD film with oleic acid ligands (upper left) undergoes a solid-state exchange to EDT ligands (upper right). The film is then infused with elemental sulfur via electron beam evaporation (lower right), resulting in a stoichiometry-tuned film (lower left). (b) A truncated cross-sectional schematic of a single PbS CQD with EDT ligands only (top) and after sulfur infusion (bottom). Empty Pb-bonding sites are partially filled with sulfur atoms, as indicated by the red outlines.

saturates, however, beyond a hole mobility of approximately 5 × 10^{-4} cm^2 V^{-1} s^{-1}; increasing the hole mobility in the HTL beyond this value has a minimal impact on the performance of the solar cell for all values of the doping density. We note that most currently used HTLs in CQD solar cells are reported to have hole mobilities greater than 5 × 10^{-4} cm^2 V^{-1} s^{-1}, as will be discussed in the context of our experimental results below.

More surprisingly, we also observe an increase in PCE with increasing electron mobility of the HTL from 5 × 10^{-4} to 5 × 10^{-1} cm^2 V^{-1} s^{-1}, as seen in Figure 1d, with the hole mobility set to our experimental value of 5 × 10^{-2} cm^2 V^{-1} s^{-1}. This can be mostly attributed to an increase in the short-circuit current (J_{SC}), as seen in Figure 1e. We also observe that when the electron mobility becomes greater than the hole mobility used in the simulations (5 × 10^{-1} cm^2 V^{-1} s^{-1}), the performance of the solar cell begins to decline.

The improved device performance associated with increasing electron mobility in the HTL is an unexpected result. The electron mobility in the HTL should have a negligible impact on device performance under ideal circumstances, given that the function of the HTL is to block electrons and transport holes only. We hypothesize that this could mean that significant photogeneration happens in the HTL such that this layer also plays a non-negligible role in electron transport. Similar photogeneration observations have previously been attributed to optical interference effects at the top contact interface.[39]

We tested this hypothesis by running a series of simulations in which we varied the thickness of the PbS-PbX_2 absorbing layer to see if there was a point at which the electron mobility of the HTL no longer played a significant role in device performance. The results are shown in Figure 1f. We varied the electron mobility in the HTL from 5 × 10^{-4} to 5 × 10^{-2} cm^2 V^{-1} s^{-1} and the absorbing layer thickness from 300 to 900 nm. At our experimental value of the absorbing layer thickness, 350 nm, increasing the electron mobility in the HTL has a strong positive effect on PCE. However, as the absorbing layer thickness increases, the impact of electron mobility decreases and becomes negligible at absorbing layer thicknesses of larger than approximately 500 nm, where the device performances peaks. We further confirmed our hypothesis that significant photogeneration is predicted to occur in the HTL by using transfer-matrix method calculations[40] to quantify the spatial electric field profile in our device. We found that 10.2% of the optical total absorption occurs in the HTL, as can be seen in Figure S3. This roughly matches with the predicted improvement in J_{SC} due to improvements in electron mobility in the HTL (Figure 1e).

We also performed band structure simulations to determine the optimal alignment between the absorbing layer and the HTL. We varied the valence band edge energy difference between the HTL and the absorbing layer from zero to 0.4 eV, with the HTL valence band edge assumed to be shallower than the absorbing layer edge. The results are shown in Figure S2. We found that for the standard (PbS-EDT) HTL (doping density of 2.54 × 10^{17} cm^{-3}, hole mobility of 5.58 × 10^{-2} cm^2 V^{-1} s^{-1}, and electron mobility of 1.05 × 10^{-3} cm^2 V^{-1} s^{-1}), the optimal valence band energy difference is approximately 0.15 eV. For an optimized HTL (doping density of 1.10 × 10^{18} cm^{-3}, hole mobility of 5.23 × 10^{-2} cm^2 V^{-1} s^{-1}, and electron mobility of 1.65 × 10^{-2} cm^2 V^{-1} s^{-1}), the optimal valence band energy difference is approximately 0.23 eV. Full SCAPS results for the band structures of different device configurations are shown in Figure 4b.

To summarize the results of our SCAPS simulations, we found that, given the current properties of the absorbing layer, a good HTL needs a doping density of at least 10^{18} cm^{-3}, an electron mobility greater than 5 × 10^{-2} cm^2 V^{-1} s^{-1}, a hole mobility greater than 5 × 10^{-4} cm^2 V^{-1} s^{-1}, and a valence band edge difference between the absorbing layer and the HTL of approximately 0.23 eV. We therefore sought to design and fabricate a new material that was compatible with standard CQD solar cell fabrication methods while fulfilling the above requirements. This led us to explore elemental sulfur infusion of the PbS-EDT materials, which has been previously shown to improve carrier mobilities and increase p-type doping density

https://dx.doi.org/10.1021/acsenergylett.0c01586
ACS Energy Lett. 2020, 5, 2897−2904

Table 1. Summary of CQD Solar Cell Performance[a]

device	PCE [%], best (average)	V_{OC} [V], best (average)	J_{SC} [mA cm^{-2}], best (average)	fill factor, best (average)
no Sulfur	9.32 (7.51 ± 0.98)	0.57 (0.56 ± 0.01)	25.61 (21.32 ± 2.50)	0.61 (0.61 ± 0.01)
1 Å sulfur	9.16 (7.72 ± 0.95)	0.58 (0.57 ± 0.01)	24.97 (21.63 ± 2.65)	0.62 (0.61 ± 0.01)
3 Å sulfur	9.22 (7.79 ± 1.2)	0.58 (0.57 ± 0.01)	23.79 (21.22 ± 2.71)	0.64 (0.61 ± 0.03)
6 Å sulfur	9.80 (8.67 ± 0.39)	0.57 (0.57 ± 0.00)	25.72 (23.84 ± 1.00)	0.65 (0.62 ± 0.02)
9 Å sulfur	9.97 (9.04 ± 0.74)	0.58 (0.58 ± 0.01)	26.21 (24.07 ± 1.84)	0.64 (0.63 ± 0.01)
15 Å sulfur	10.35 (9.00 ± 0.62)	0.58 (0.57 ± 0.00)	26.51 (24.17 ± 1.47)	0.65 (0.63 ± 0.01)

[a]Measured over a total of 246 solar cells; 30−59 for each row.

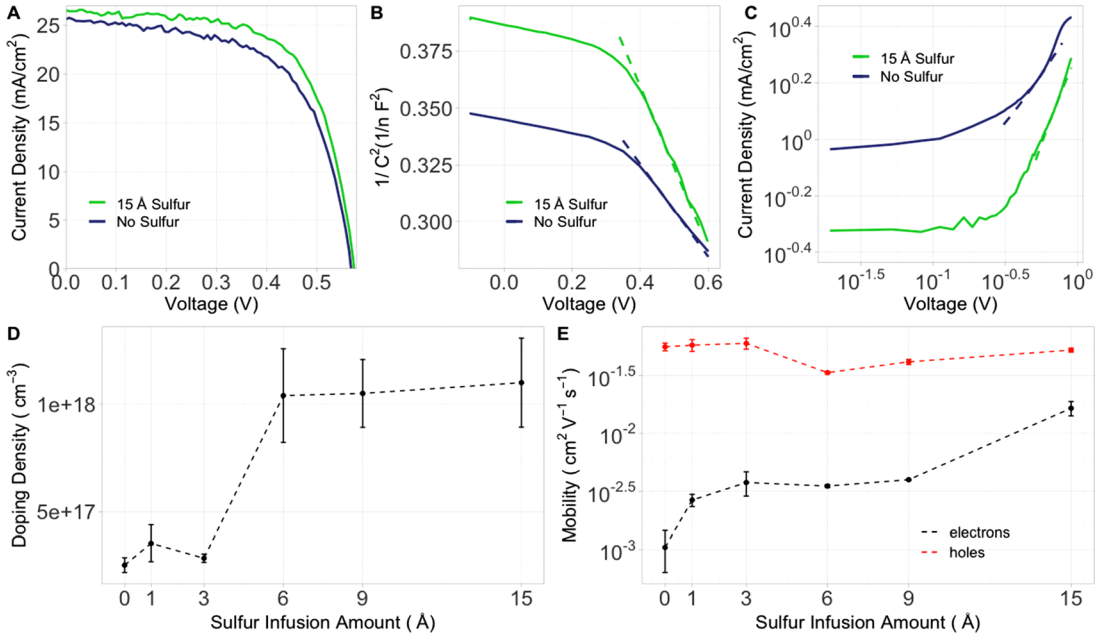

Figure 3. (a) Current density−voltage plots of the best performing control HTL device (purple) and a 15 Å sulfur HTL device (green). (b) Cap−*V* measurement results of a control HTL device (purple) and a 15 Å sulfur HTL device (green) and the fit lines used to extract the doping densities (dashed). (c) Current−voltage log plot of an electron-transport SCLC structure control HTL device (purple) and a 15 Å sulfur HTL device (green), with the SCLC region, used to calculate the electron mobility, indicated by dashed lines. (d) Average doping density in the HTL extracted from Cap−*V* measurements as a function of HTL sulfur infusion amount. (e) Hole mobility (red) and electron mobility (black) extracted from SCLC measurements as a function of HTL sulfur infusion amount.

in CQD field effect transistors.[41] We hypothesized that introducing elemental sulfur into the PbS-EDT materials would allow us to control the stoichiometry of the CQDs that comprise the HTL, reducing the density of surface traps that limit carrier mobilities while fine-tuning the band edge energies and Fermi level.

We used electron beam evaporation to infuse elemental sulfur into the standard PbS-EDT HTL, keeping all other device fabrication procedures the same as in previous reports[19,42,43] and as described in Experimental Methods in the Supporting Information. The experimental procedure is illustrated schematically in Figure 2a. We tested effective sulfur thicknesses of 1, 3, 6, 9, and 15 Å, as monitored using the built-in quartz crystal oscillator in our electron beam evaporator. We estimate that an effective evaporation thickness of 15 Å of sulfur corresponds to roughly 30 atoms of sulfur per nanocrystal on average, using the following assumptions: The HTL CQD films have a density of roughly 1.8×10^{14} nanocrystals/cm^2, assuming a face-centered cubic packing profile derived from TEM images, and a layer thickness of approximately 60 nm; the density of the cubic close-packed structure of sulfur yields about 3.13×10^{22} atoms/cm^3.

We measured current-density−voltage characteristics under simulated AM1.5G solar illumination of our solar cells with different HTLs to extract the relevant solar cell device parameters. From the results shown in Table 1, we see that there is a gradual increase in CQD solar cell PCE that plateaus with an increasing amount of sulfur, up to 15 Å. Comparing the best performing sulfur-infused solar cell, with 15 Å of sulfur, to our control device with no sulfur infusion, we see an absolute increase of 1% in the PCE, from 9.32% to 10.35%, a relative increase of 11% (Figure 3a), and an absolute average increase of 1.5% from 7.51% to 9.00%. Consistent with our SCAPS simulation results, the increase in the PCE is due to increases in both the fill factor and the short-circuit current, while the open-circuit voltage is relatively unaffected by sulfur-infusion of the HTL.

To verify that the increase in PCE was primarily a result of an increase in the doping density and electron mobility of the HTL, we used Cap−*V* measurements and SCLC measurements, respectively, to characterize our different HTLs. Using Cap−*V* measurements, we extracted an average doping density of 2.5×10^{17} cm^{-3} for the PbS-EDT HTL in our control devices without sulfur addition and an average doping density of 1.1×10^{18} cm^{-3} for the 15 Å sulfur-infused HTL. We found

https://dx.doi.org/10.1021/acsenergylett.0c01586
ACS Energy Lett. 2020, 5, 2897−2904

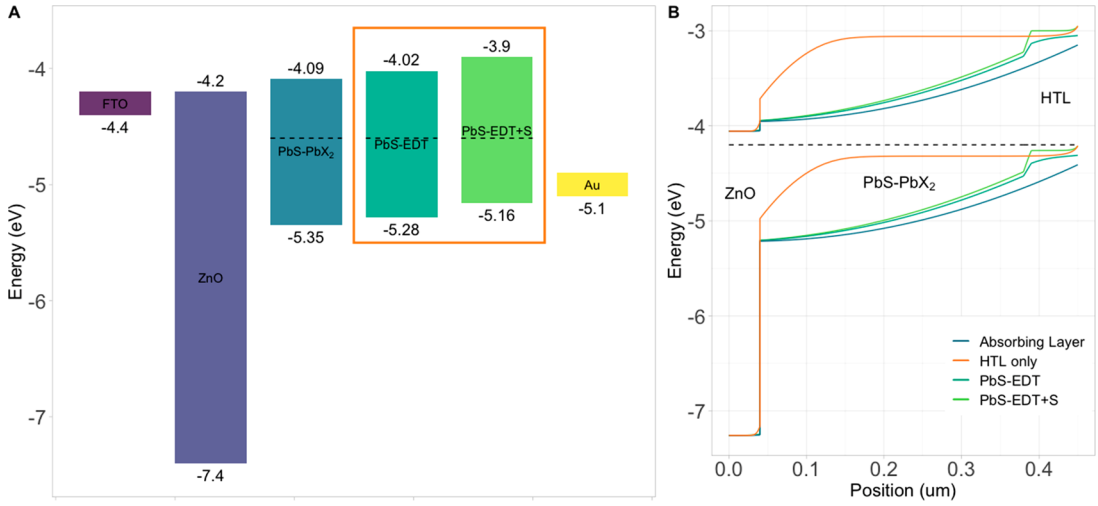

Figure 4. (a) Band diagram for a PbS CQD solar cell, with the HTL layer alternatives highlighted by the orange box. Band edge positions are taken from the literature (FTO,[48] ZnO[34], and Au[49]) and extracted from UPS and UV−vis−NIR spectrophotometric absorption measurements (PbS-PbX_2, PbS-EDT, and PbS-EDT+S). (b) SCAPS simulated band diagrams at equilibrium for different solar cell devices: the full structure shown in Figure 1c with a sulfur-infused HTL (light green), the full structure with a nonsulfur-infused HTL (dark green), a device with an absorbing layer but no HTL (blue), and a device with a nonsulfur-infused HTL but no absorbing layer (orange). The Fermi level is indicated by the black dashed line, and regions corresponding to the different layers of the solar cell are indicated.

that there was a notable increase in the doping density as the amount of sulfur in the HTL was increased from 3 to 6 Å (Figure 3b,d), which correlated with a similar trend in the PCE. The largest PCE increase, from 9.2% to 9.8% for the best performing solar cells of each type and from 7.8% to 8.7% for the average of each type of cell, occurred as the amount of sulfur in the HTL was increased from 3 to 6 Å.

We performed ultraviolet photoelectron spectroscopy (UPS) measurements (Figure S4) to determine the location of the valence band edges of the HTL and absorbing layer materials and to verify any band structure shifts from the sulfur-infusion-induced modification of the CQD surface structure, as illustrated in Figure 2b. We found that the control PbS-EDT HTL had a valence band edge that was approximately 0.07 eV shallower than that of the absorbing CQD layer. The difference for the 15 Å sulfur-infused HTL and the absorbing CQD layer increased to about 0.12 eV (Figure 4a). We note that both of these energy differences are approximately 0.1 eV smaller than the ideal band alignment predicted by our SCAPS simulations for their relative doping densities (Figure S2).

We used space-charge-limited current (SCLC) measurements to measure the carrier mobilities in our HTL[44,45] (Figure 3c,e). The SCLC method uses a device architecture with the semiconductor material of interest inserted between one charge injection contact and one injection-blocking electrode to ensure that current in the device is due to only one carrier type.[35,38] Dark current−voltage curves are measured, and carrier mobility is extracted by fitting the SCLC region, where there is a quadratic relationship between the applied current and voltage. In this regime, charges tend to accumulate in the region between the electrodes, and the electric field, and thus the current, is dependent on only the carrier mobility, which can be extracted using the Mott−Gurney Law. For hole mobility measurements, we used an ITO bottom contact, a poly(3,4-ethylenedioxythiophene) polystyrene sulfonate (PEDOT:PSS) layer, the semiconducting test layer (either the HTL or absorbing PbS CQD layer), and a Au top contact. The hole mobility results for a range of sulfur infusion conditions are shown in Figure 3e. We found that sulfur infusion had a minimal impact on hole mobility, with all results on the order of 10^{-2} cm^2 V^{-1} s^{-1}, 2 orders of magnitude greater than the threshold required for PCE saturation of 5×10^{-4} cm^2 V^{-1} s^{-1}, which was calculated assuming the control experimental values of the electron mobility and doping density.

For electron mobility measurements, our device architecture consisted of a fluorine-doped tin oxide (FTO) bottom contact, a ZnO anode, the semiconducting test layer (either the HTL or absorbing PbS CQD layer), and a Au top contact. We measured a gradual increase in the electron mobility as the amount of sulfur in the HTL was increased, totaling an order of magnitude increase from an average of 1.05×10^{-3} cm^2 V^{-1} s^{-1} to 1.65×10^{-2} cm^2 V^{-1} s^{-1}, for the control HTL device with no sulfur and the device with 15 Å of sulfur in the HTL, respectively. We posit that the increase in effective electron mobility could arise from sulfur passivation of the surface trap states of the EDT-ligated CQDs, as has been previously observed.[20,46,47]

We also performed external quantum efficiency (EQE) measurements (Figure S5), which confirmed our experimental results, even after several months of device aging. There is an overall improvement in the current across all wavelengths with the addition of sulfur to the HTL, which is likely a result of the higher doping density in the HTL and consequent larger charge-extracting drift field. There is an additional current enhancement at the exciton peak wavelength, which could be attributed to better collection of longer-wavelength photons, which are more likely to be absorbed near the back of the device, because of the improved HTL electron mobility.

Our experimental results confirmed the predictions from the SCAPS simulations. The primary effect of the sulfur infusion was to increase the doping density and electron mobility in the HTL compared to the control PbS-EDT HTL. The increase in both of these properties correlated with an increase in solar cell PCE, primarily through increases in the short-circuit current and fill factor, as expected.

https://dx.doi.org/10.1021/acsenergylett.0c01586
ACS Energy Lett. 2020, 5, 2897−2904

To summarize, we set out to understand the requirements of a good HTL for CQD solar cells and to develop a new strategy to implement these requirements. Using 1D SCAPS simulations, we studied the effects of the HTL doping density, carrier mobility, and relative band edge locations on device performance. We found that the hole mobilities in current HTL materials are predicted to be sufficient for high efficiency and are not currently the limiting factor in performance. Instead, we found that increasing the doping density in the HTL by an order of magnitude should have a significant effect on PCE, and counterintuitively, low electron mobility in the HTL was limiting performance because of a significant amount of photogeneration occurring in the HTL. We then developed a new strategy to address these limitations: sulfur infusion of the traditional PbS-EDT HTL to increase the p-type character by shifting the stoichiometry of the film and improving the electron mobility through passivation of surface electron trap states. We demonstrated that our new HTL behaved as predicted, achieving an average absolute increase of 1.5% in the PCE over solar cells with the PbS-EDT HTL.

This work points to new directions for further improvements in CQD solar cell PCE through engineering of both the HTL and CQD absorbing layer properties. Specifically, carrier transport in the CQD absorbing layer should be improved so that this layer can be made thick enough such that significant photogeneration does not need to occur in the HTL.

■ ASSOCIATED CONTENT

Supporting Information

The Supporting Information is available free of charge at https://pubs.acs.org/doi/10.1021/acsenergylett.0c01586.

Experimental methods, full SCAPS simulation results and parameters, transfer matrix method calculation results on absorption and generation, ultraviolet photoelectron spectroscopy and UV−vis spectrophotometry measurements, and external quantum efficiency measurements (PDF)

■ AUTHOR INFORMATION

Corresponding Author

Susanna M. Thon − *Department of Electrical and Computer Engineering, Johns Hopkins University, Baltimore, Maryland 21218, United States;* orcid.org/0000-0002-1003-2650; Email: susanna.thon@jhu.edu

Authors

Arlene Chiu − *Department of Electrical and Computer Engineering, Johns Hopkins University, Baltimore, Maryland 21218, United States;* orcid.org/0000-0002-7009-4984

Eric Rong − *Department of Electrical and Computer Engineering, Johns Hopkins University, Baltimore, Maryland 21218, United States*

Christianna Bambini − *Department of Electrical and Computer Engineering, Johns Hopkins University, Baltimore, Maryland 21218, United States*

Yida Lin − *Department of Electrical and Computer Engineering, Johns Hopkins University, Baltimore, Maryland 21218, United States*

Chengchangfeng Lu − *Department of Electrical and Computer Engineering, Johns Hopkins University, Baltimore, Maryland 21218, United States*

Complete contact information is available at: https://pubs.acs.org/10.1021/acsenergylett.0c01586

Notes

The authors declare no competing financial interest.

■ ACKNOWLEDGMENTS

This work was supported by the National Science Foundation (DMR-1807342). The authors thank Huy Vo for guidance in the sulfur evaporation process and Hugo Celio for UPS measurements.

■ REFERENCES

(1) Bawendi, M. G.; Steigerwald, M. L.; Brus, L. E. The Quantum Mechanics of Larger Semiconductor Clusters ("Quantum Dots"). *Annu. Rev. Phys. Chem.* **1990**, *41*, 477−496.

(2) Song, J. H.; Jeong, S. Colloidal Quantum Dot Based Solar Cells: From Materials to Devices. *Nano Converg.* **2017**, *4*, 21.

(3) Shirasaki, Y.; Supran, G. J.; Bawendi, M. G.; Bulović, V. Emergence of Colloidal Quantum-Dot Light-Emitting Technologies. *Nat. Photonics* **2013**, *7*, 13−23.

(4) Yang, Z.; Gao, M.; Wu, W.; Yang, X.; Sun, X. W.; Zhang, J.; Wang, H.-C.; Liu, R.-S.; Han, C.-Y.; Yang, H.; Li, W. Recent Advances in Quantum Dot-Based Light-Emitting Devices: Challenges and Possible Solutions. *Mater. Today* **2019**, *24*, 69−93.

(5) Hines, M. A.; Scholes, G. D. Colloidal PbS Nanocrystals with Size-Tunable Near-Infrared Emission: Observation of Post-Synthesis Self-Narrowing of the Particle Size Distribution. *Adv. Mater.* **2003**, *15*, 1844−1849.

(6) Kramer, I. J.; Minor, J. C.; Moreno-Bautista, G.; Rollny, L.; Kanjanaboos, P.; Kopilovic, D.; Thon, S. M.; Carey, G. H.; Chou, K. W.; Zhitomirsky, D.; Amassian, A.; Sargent, E. H. Efficient Spray-Coated Colloidal Quantum Dot Solar Cells. *Adv. Mater.* **2015**, *27*, 116−121.

(7) Loiudice, A.; Rizzo, A.; Corricelli, M.; Curri, M. L.; Belviso, M. R.; Cozzoli, P. D.; Grancini, G.; Petrozza, A.; Gigli, G. Room-Temperature Treatments for All-Inorganic Nanocrystal Solar Cell Devices. *Thin Solid Films* **2014**, *560*, 44−48.

(8) Wang, X.; Koleilat, G. I.; Tang, J.; Liu, H.; Kramer, I. J.; Debnath, R.; Brzozowski, L.; Barkhouse, D. A. R.; Levina, L.; Hoogland, S.; Sargent, E. H. Tandem Colloidal Quantum Dot Solar Cells Employing a Graded Recombination Layer. *Nat. Photonics* **2011**, *5*, 480−484.

(9) Manekkathodi, A.; Chen, B.; Kim, J.; Baek, S.-W.; Scheffel, B.; Hou, Y.; Ouellette, O.; Saidaminov, M. I.; Voznyy, O.; Madhavan, V. E.; Belaidi, A.; Ashhab, S.; Sargent, E. Solution-Processed Perovskite-Colloidal Quantum Dot Tandem Solar Cells for Photon Collection beyond 1000 Nm. *J. Mater. Chem. A* **2019**, *7*, 26020−26028.

(10) Arinze, E. S.; Qiu, B.; Palmquist, N.; Cheng, Y.; Lin, Y.; Nyirjesy, G.; Qian, G.; Thon, S. M. Color-Tuned and Transparent Colloidal Quantum Dot Solar Cells via Optimized Multilayer Interference. *Opt. Express* **2017**, *25*, A101−A112.

(11) Hestnes, A. G. Building Integration of Solar Energy Systems. *Sol. Energy* **1999**, *67*, 181−187.

(12) He, J.; Luo, M.; Hu, L.; Zhou, Y.; Jiang, S.; Song, H.; Ye, R.; Chen, J.; Gao, L.; Tang, J. Flexible Lead Sulfide Colloidal Quantum Dot Photodetector Using Pencil Graphite Electrodes on Paper Substrates. *J. Alloys Compd.* **2014**, *596*, 73−78.

(13) Kramer, I. J.; Moreno-Bautista, G.; Minor, J. C.; Kopilovic, D.; Sargent, E. H. Colloidal Quantum Dot Solar Cells on Curved and Flexible Substrates. *Appl. Phys. Lett.* **2014**, *105*, 163902.

(14) Choi, M.-J.; García de Arquer, F. P.; Proppe, A. H.; Seifitokaldani, A.; Choi, J.; Kim, J.; Baek, S.-W.; Liu, M.; Sun, B.; Biondi, M.; Scheffel, B.; Walters, G.; Nam, D.-H.; Jo, J. W.; Ouellette, O.; Voznyy, O.; Hoogland, S.; Kelley, S. O.; Jung, Y. S.; Sargent, E. H. Cascade Surface Modification of Colloidal Quantum Dot Inks Enables Efficient Bulk Homojunction Photovoltaics. *Nat. Commun.* **2020**, *11*, 103.

(15) Zhang, J.; Gao, J.; Miller, E. M.; Luther, J. M.; Beard, M. C. Diffusion-Controlled Synthesis of PbS and PbSe Quantum Dots with *in Situ* Halide Passivation for Quantum Dot Solar Cells. *ACS Nano* **2014**, *8*, 614−622.
(16) Yuan, M.; Kemp, K. W.; Thon, S. M.; Kim, J. Y.; Chou, K. W.; Amassian, A.; Sargent, E. H. High-Performance Quantum-Dot Solids via Elemental Sulfur Synthesis. *Adv. Mater.* **2014**, *26*, 3513−3519.
(17) Maraghechi, P.; Labelle, A. J.; Kirmani, A. R.; Lan, X.; Adachi, M. M.; Thon, S. M.; Hoogland, S.; Lee, A.; Ning, Z.; Fischer, A.; Amassian, A.; Sargent, E. H. The Donor−Supply Electrode Enhances Performance in Colloidal Quantum Dot Solar Cells. *ACS Nano* **2013**, *7*, 6111−6116.
(18) Chuang, C.-H. M.; Brown, P. R.; Bulović, V.; Bawendi, M. G. Improved Performance and Stability in Quantum Dot Solar Cells through Band Alignment Engineering. *Nat. Mater.* **2014**, *13*, 796−801.
(19) Ip, A. H.; Thon, S. M.; Hoogland, S.; Voznyy, O.; Zhitomirsky, D.; Debnath, R.; Levina, L.; Rollny, L. R.; Carey, G. H.; Fischer, A.; Kemp, K. W.; Kramer, I. J.; Ning, Z.; Labelle, A. J.; Chou, K. W.; Amassian, A.; Sargent, E. H. Hybrid Passivated Colloidal Quantum Dot Solids. *Nat. Nanotechnol.* **2012**, *7*, 577−582.
(20) Tang, J.; Kemp, K. W.; Hoogland, S.; Jeong, K. S.; Liu, H.; Levina, L.; Furukawa, M.; Wang, X.; Debnath, R.; Cha, D.; Chou, K. W.; Fischer, A.; Amassian, A.; Asbury, J. B.; Sargent, E. H. Colloidal-Quantum-Dot Photovoltaics Using Atomic-Ligand Passivation. *Nat. Mater.* **2011**, *10*, 765−771.
(21) Green, M. A.; Dunlop, E. D.; Hohl-Ebinger, J.; Yoshita, M.; Kopidakis, N.; Ho-Baillie, A. W. Y. Solar Cell Efficiency Tables (Version 55). *Prog. Photovoltaics* **2020**, *28*, 3−15.
(22) Liu, M.; Voznyy, O.; Sabatini, R.; García de Arquer, F. P.; Munir, R.; Balawi, A. H.; Lan, X.; Fan, F.; Walters, G.; Kirmani, A. R.; Hoogland, S.; Laquai, F.; Amassian, A.; Sargent, E. H. Hybrid Organic−Inorganic Inks Flatten the Energy Landscape in Colloidal Quantum Dot Solids. *Nat. Mater.* **2017**, *16*, 258−263.
(23) Wang, H.; Gonzalez-Pedro, V.; Kubo, T.; Fabregat-Santiago, F.; Bisquert, J.; Sanehira, Y.; Nakazaki, J.; Segawa, H. Enhanced Carrier Transport Distance in Colloidal PbS Quantum-Dot-Based Solar Cells Using ZnO Nanowires. *J. Phys. Chem. C* **2015**, *119*, 27265−27274.
(24) Lan, X.; Voznyy, O.; Kiani, A.; García de Arquer, F. P.; Abbas, A. S.; Kim, G.-H.; Liu, M.; Yang, Z.; Walters, G.; Xu, J.; Yuan, M.; Ning, Z.; Fan, F.; Kanjanaboos, P.; Kramer, I.; Zhitomirsky, D.; Lee, P.; Perelgut, A.; Hoogland, S.; Sargent, E. H. Passivation Using Molecular Halides Increases Quantum Dot Solar Cell Performance. *Adv. Mater.* **2016**, *28*, 299−304.
(25) Willis, S. M.; Cheng, C.; Assender, H. E.; Watt, A. A. R. The Transitional Heterojunction Behavior of PbS/ZnO Colloidal Quantum Dot Solar Cells. *Nano Lett.* **2012**, *12*, 1522−1526.
(26) Litvin, A. P.; Martynenko, I. V.; Purcell-Milton, F.; Baranov, A. V.; Fedorov, A. V.; Gun'ko, Y. K. Colloidal Quantum Dots for Optoelectronics. *J. Mater. Chem. A* **2017**, *5*, 13252−13275.
(27) Lin, Y.; Ung, G.; Qiu, B.; Qian, G.; Thon, S. M. Integrated Concentrators for Scalable High-Power Generation from Colloidal Quantum Dot Solar Cells. *ACS Appl. Energy Mater.* **2018**, *1*, 2592−2599.
(28) Biondi, M.; Choi, M.-J.; Ouellette, O.; Baek, S.-W.; Todorović, P.; Sun, B.; Lee, S.; Wei, M.; Li, P.; Kirmani, A. R.; Sagar, L. K.; Richter, L. J.; Hoogland, S.; Lu, Z.-H.; García de Arquer, F. P.; Sargent, E. H. A Chemically Orthogonal Hole Transport Layer for Efficient Colloidal Quantum Dot Solar Cells. *Adv. Mater.* **2020**, *32*, 1906199.
(29) Teh, Z. L.; Hu, L.; Zhang, Z.; Gentle, A. R.; Chen, Z.; Gao, Y.; Yuan, L.; Hu, Y.; Wu, T.; Patterson, R. J.; Huang, S. Enhanced Power Conversion Efficiency via Hybrid Ligand Exchange Treatment of P-Type PbS Quantum Dots. *ACS Appl. Mater. Interfaces* **2020**, *12*, 22751−22759.
(30) Burgelman, M.; Nollet, P.; Degrave, S. Modelling Polycrystalline Semiconductor Solar Cells. *Thin Solid Films* **2000**, *361*−*362*, 527−532.
(31) Oh, S. J.; Berry, N. E.; Choi, J.-H.; Gaulding, E. A.; Paik, T.; Hong, S.-H.; Murray, C. B.; Kagan, C. R. Stoichiometric Control of Lead Chalcogenide Nanocrystal Solids to Enhance Their Electronic and Optoelectronic Device Performance. *ACS Nano* **2013**, *7*, 2413−2421.
(32) Ray, J.; Chaudhuri, T. K.; Panchal, C.; Patel, K.; Patel, K.; Bhatt, G.; Suryavanshi, P. PbS-ZnO Solar Cell: A Numerical Simulation. *J. Nano- Electron. Phys.* **2017**, *9*, 03041-1.
(33) Sharma, A.; Yadav, R. S.; Pandey, B. P. Performance Analysis of PbS Colloidal Quantum Dot Solar Cell at Different Absorption Coefficient. *J. Energy Environ. Sustain.* **2019**, *7*, 32−35.
(34) Zhang, X.; Johansson, E. M. J. Reduction of Charge Recombination in PbS Colloidal Quantum Dot Solar Cells at the Quantum Dot/ZnO Interface by Inserting a MgZnO Buffer Layer. *J. Mater. Chem. A* **2017**, *5*, 303−310.
(35) Cho, Y.; Hou, B.; Lim, J.; Lee, S.; Pak, S.; Hong, J.; Giraud, P.; Jang, A.-R.; Lee, Y.-W.; Lee, J.; Jang, J. E.; Snaith, H. J.; Morris, S. M.; Sohn, J. I.; Cha, S.; Kim, J. M. Balancing Charge Carrier Transport in a Quantum Dot P−N Junction toward Hysteresis-Free High-Performance Solar Cells. *ACS Energy Lett.* **2018**, *3*, 1036−1043.
(36) Huang, S.; Hu, L.; Patterson, R.; Zhang, Z.; Yuan, L.; Chen, W.; Hu, Y.; Chen, Z.; Gao, Y.; Teh, Z. L.; Yan, C.; Conibeer, G. J. Improving Hole Extraction for PbS Quantum Dot Solar Cells. In 2018 *IEEE 7th World Conference on Photovoltaic Energy Conversion (WCPEC) (A Joint Conference of 45th IEEE PVSC, 28th PVSEC & 34th EU PVSEC)*, Waikoloa Village, HI, June 10−15, 2018; pp 2756−2758.
(37) Gu, M.; Wang, Y.; Yang, F.; Lu, K.; Xue, Y.; Wu, T.; Fang, H.; Zhou, S.; Zhang, Y.; Ling, X.; Xu, Y.; Li, F.; Yuan, J.; Loi, M. A.; Liu, Z.; Ma, W. Stable PbS Quantum Dot Ink for Efficient Solar Cells by Solution-Phase Ligand Engineering. *J. Mater. Chem. A* **2019**, *7*, 15951−15959.
(38) Speirs, M. J.; Dirin, D. N.; Abdu-Aguye, M.; Balazs, D. M.; Kovalenko, M. V.; Loi, M. A. Temperature Dependent Behaviour of Lead Sulfide Quantum Dot Solar Cells and Films. *Energy Environ. Sci.* **2016**, *9*, 2916−2924.
(39) Ouellette, O.; Lesage-Landry, A.; Scheffel, B.; Hoogland, S.; García de Arquer, F. P.; Sargent, E. H. Spatial Collection in Colloidal Quantum Dot Solar Cells. *Adv. Funct. Mater.* **2020**, *30*, 1908200.
(40) Burkhard, G. F.; Hoke, E. T.; McGehee, M. D. Accounting for Interference, Scattering, and Electrode Absorption to Make Accurate Internal Quantum Efficiency Measurements in Organic and Other Thin Solar Cells. *Adv. Mater.* **2010**, *22*, 3293−3297.
(41) Balazs, D. M.; Bijlsma, K. I.; Fang, H.-H.; Dirin, D. N.; Döbeli, M.; Kovalenko, M. V.; Loi, M. A. Stoichiometric Control of the Density of States in PbS Colloidal Quantum Dot Solids. *Sci. Adv.* **2017**, *3*, eaao1558.
(42) Liu, L.; Bisri, S. Z.; Ishida, Y.; Hashizume, D.; Aida, T.; Iwasa, Y. Ligand and Solvent Effects on Hole Transport in Colloidal Quantum Dot Assemblies for Electronic Devices. *ACS Appl. Nano Mater.* **2018**, *1*, 5217−5225.
(43) Xu, J.; Voznyy, O.; Liu, M.; Kirmani, A. R.; Walters, G.; Munir, R.; Abdelsamie, M.; Proppe, A. H.; Sarkar, A.; García de Arquer, F. P.; Wei, M.; Sun, B.; Liu, M.; Ouellette, O.; Quintero-Bermudez, R.; Li, J.; Fan, J.; Quan, L.; Todorovic, P.; Tan, H.; Hoogland, S.; Kelley, S. O.; Stefik, M.; Amassian, A.; Sargent, E. H. 2D Matrix Engineering for Homogeneous Quantum Dot Coupling in Photovoltaic Solids. *Nat. Nanotechnol.* **2018**, *13*, 456−462.
(44) Kwan Kim, J.; Hoon Song, J.; Choi, H.; Jae Baik, S.; Jeong, S. Space Charge Limited Conduction in Ultrathin PbS Quantum Dot Solid Diodes. *J. Appl. Phys.* **2014**, *115*, No. 054302.
(45) Rath, A. K.; Lasanta, T.; Bernechea, M.; Diedenhofen, S. L.; Konstantatos, G. Determination of Carrier Lifetime and Mobility in Colloidal Quantum Dot Films via Impedance Spectroscopy. *Appl. Phys. Lett.* **2014**, *104*, No. 063504.
(46) Jeong, K. S.; Tang, J.; Liu, H.; Kim, J.; Schaefer, A. W.; Kemp, K.; Levina, L.; Wang, X.; Hoogland, S.; Debnath, R.; Brzozowski, L.; Sargent, E. H.; Asbury, J. B. Enhanced Mobility-Lifetime Products in

https://dx.doi.org/10.1021/acsenergylett.0c01586
ACS Energy Lett. 2020, 5, 2897−2904

PbS Colloidal Quantum Dot Photovoltaics. *ACS Nano* **2012**, *6*, 89−99.
(47) Barkhouse, D. A. R.; Pattantyus-Abraham, A. G.; Levina, L.; Sargent, E. H. Thiols Passivate Recombination Centers in Colloidal Quantum Dots Leading to Enhanced Photovoltaic Device Efficiency. *ACS Nano* **2008**, *2*, 2356−2362.
(48) Helander, M. G.; Greiner, M. T.; Wang, Z. B.; Tang, W. M. Work Function of Fluorine Doped Tin Oxide. *J. Vac. Sci. Technol., A* **2011**, *29*, No. 011019.
(49) Sachtler, W. M. H.; Dorgelo, G. J. H.; Holscher, A. A. The Work Function of Gold. *Surf. Sci.* **1966**, *5*, 221−229.

https://dx.doi.org/10.1021/acsenergylett.0c01586
ACS Energy Lett. 2020, 5, 2897−2904